nature portfolio

https://doi.org/10.1038/s41586-024-07454-5

Supplementary information

Reproducible graphene synthesis by oxygen-free chemical vapour deposition

In the format provided by the authors and unedited

Supplementary Information for Reproducible graphene synthesis by oxygen-free chemical vapor deposition

Jacob Amontree[1†], Xingzhou Yan[1†], Christopher S. DiMarco[1†], Pierre L. Levesque[2,3], Tehseen Adel[4], Jordan Pack[5], Madisen Holbrook[5], Christian Cupo[1], Zhiying Wang[1], Dihao Sun[5], Adam J. Biacchi[6], Charlezetta E. Wilson-Stokes[4,7], Kenji Watanabe[8], Takashi Taniguchi[8], Cory Dean[5], Angela R. Hight Walker[4], Katayun Barmak[9*], Richard Martel[3*], James Hone[1*]

[1]Department of Mechanical Engineering, Columbia University, 500 W 120th St., New York, 10027, NY, USA.
[2] Infinite Potential Laboratories, Waterloo, N2L 0A9, Ontario, Canada.
[3]Département de Chimie and Institut Courtois, Université de Montréal, 2900 Edouard Montpetit, Montréal, H3C 3J7, Quebec, Canada.
[4]Quantum Metrology Division, National Institute of Standards and Technology (NIST), 100 Bureau Dr., Gaithersburg, 20899, MD, USA.
[5]Department of Physics, Columbia University, 530 W 120th St., New York, 10027, NY, USA.
[6]Nanoscale Device Characterization Division, National Institute of Standards and Technology (NIST), 100 Bureau Dr., Gaithersburg, 20899, MD, USA.
[7]Department of Mechanical Engineering, Howard University, 2400 6th St. NW, Washington, 20059, DC, USA.
[8]Research Center for Functional Materials, National Institute for Materials Science, 1-1 Namiki, Tsukuba, 305-0044, Japan.
[9]Department of Applied Physics and Applied Mathematics, Columbia University, 500 W 120th St., New York, 10027, NY, USA.

*Corresponding author(s). E-mail(s): kb2612@columbia.edu; r.martel@umontreal.ca; jh2228@columbia.edu;

Table of contents for Supplementary Information

Supplementary information

System schematic

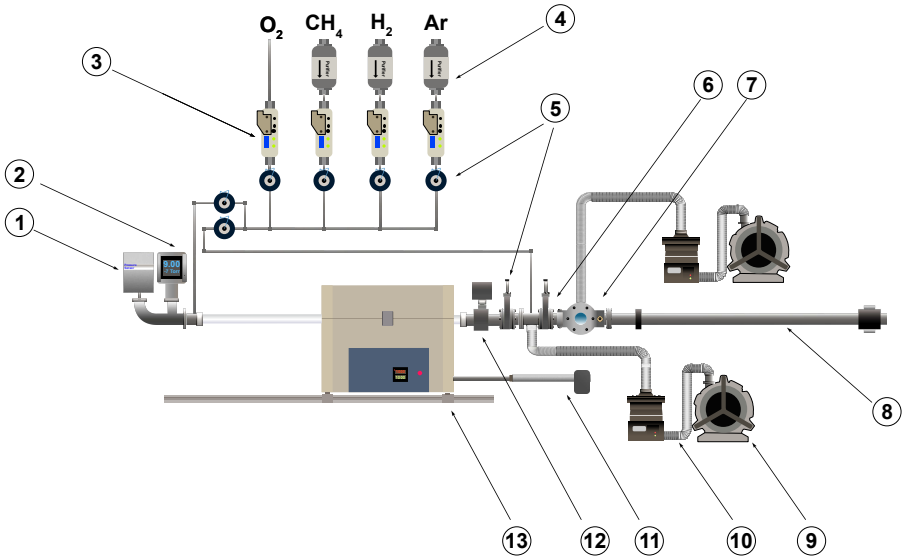

Fig. S1 CVD system overview

1. Capacitance manometer for accurate pressure measurement for growth
2. Vacuum gauge for system base pressure monitoring
3. Mass flow controller
4. Gas purifier
5. Pneumatic shut off valve
6. Pneumatic gate valve
7. Loading chamber
8. Transfer arm
9. Dry scroll pump
10. Turbomolecular pump
11. Linear actuator
12. Exhaust throttling valve
13. CVD furnace

Supplementary Note 1 - Experimental conditions

The partial pressure is calculated using Dalton's law of partial pressures. For example:

$$P_{CH_4} = P_{total} \cdot \frac{Q_{CH_4}}{Q_{CH_4} + Q_{H_2} + Q_{O_2} + Q_{Ar}} \tag{S1}$$

The mass flow controllers are calibrated to each gas composition. Here the molar ratio are estimated to be similar to the flow rate ratio. The total pressure is measured through a capacitance manometer, insensitive to the gas composition (a typical cold cathode vacuum gauge is calibrated to air, and will lead to error when measuring pressure of typical CVD gas environment).

Table S1 Experimental conditions

Figure	T_g(C)	t_g(s)	P_{Ar}(mTorr)	P_{H_2}(mTorr)	P_{CH_4}(mTorr)	P_{O_2}(μTorr)
Fig. 1b,c(top)	1000	2-120	190	0	10	0
Fig. 1b,c(bot)	1000	10-60	190	0	10	0.1
Fig. 1d,e	1050	120	76	750	4	0
Fig. 2a	1000	11-188	47.5	0	2.5	0
Fig. 2b	1000	11-28	47.5	0	2.5	0
Fig. 2c	900-1000	10	57	0	3	0
Fig. 2d	1000	8-30	47.5-98.8	0	2.5-5.2	0
Fig. 2e-1	1000	8-30	109-1658	338-1887	5.6	0
Fig. 2e-2	1000	8-30	164-1656	338-1830	8.5	0
Fig. 2e-3	1000	8-30	218-1654	338-1774	11.3	0
Fig. 2e-4	1000	8-30	168-1479	507-1718	14.1	0
Fig. 2e-5	1000	8-30	349-1081	901-1633	18.3	0
Fig. 3a-1	1000	180-720	847	150	3	0
Fig. 3a-2	1000	90-3600	847	150	3	1
Fig. 3a-3	1000	90-3600	847	150	3	4
Fig. 3a-4	1000	90-3600	847	150	3	8
Fig. 3b(top left)	1000	7200	190	500	10	0
Fig. 3b(top right)	1000	7200	190	500	10	1.32
Fig. 3b(bot left)	1000	7200	190	500	10	0
Fig. 3b(bot right)	1000	7200	190	500	10	1.32
Fig. 3c-d-1	1000	7200	190	500	10	0
Fig. 3c-d-2	1000	7200	190	500	10	0.38
Fig. 3c-d-3	1000	7200	190	500	10	0.72
Fig. 3c-d-4	1000	7200	190	500	10	1.32
Fig. 4	1000	900	190	500	10	0

OF-CVD growth temperature profile

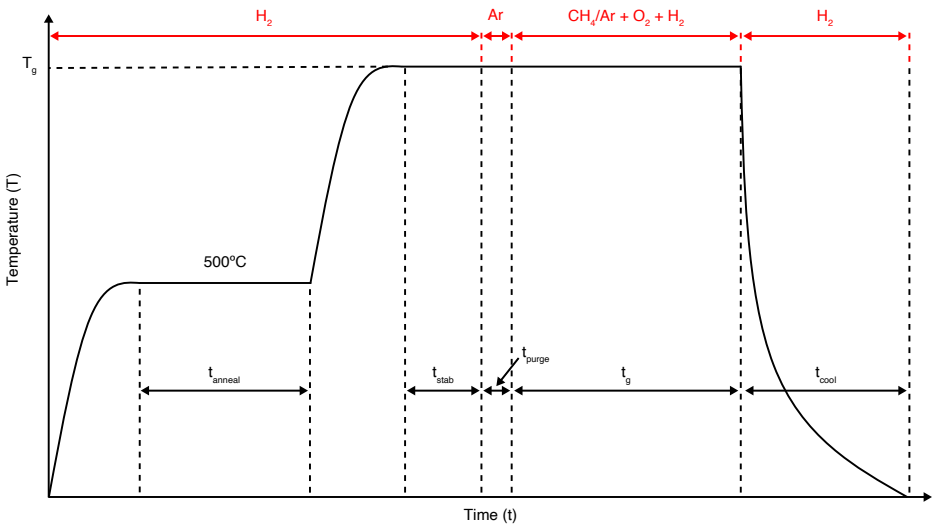

Fig. S2 Temperature profile for a typical graphene synthesis process. Gas compositions for each step are overlaid above profile.

For all experiments, t_{anneal} = 30 min, t_{stab} = 10 min, t_{purge} = 1 min. All ramp up stages are conducted with the maximum ramp rate. The time required to heat up to 500 °C from room temperature is 8 min. The time required to heat up to 1000 °C from 500 °C is 15 min.

The anneal at moderate temperature of 500 °C removes the surface oxygen and potential surface contamination prior the growth stage, while preserving the smooth surface of the Cu surface (higher temperatures will lead to more Cu sublimation in vacuum). t_{stab} before growth stage ensures the temperature is stable for the growth. Furnace is retracted right after the growth to facilitate fast cooling.

Graphene grain image processing

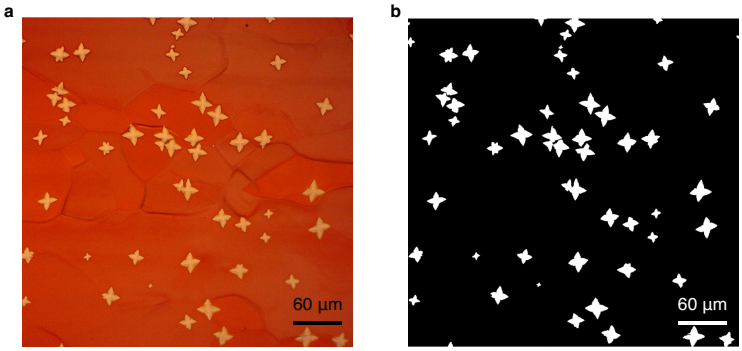

Fig. S3 Example of the grain image processing. a, original optical picture. **b**, processed image for nucleation density and grain size calculations.

MATLAB was used to create a graphene grain image processing file to automatically calculate the following quantities: number of grains per image, nucleation density (ND), average graphene grain area (GA), and total graphene coverage. If two graphene grains are merged, they are manually processed to avoid estimation errors. The Gr/Cu foil was oxidized to increase the contrast between the graphene grains and the underlying Cu substrate. The graphene covered regions are marked as white pixels through color thresholding and compared to the black background for quantitative analysis.

Optical data for reproducibility study

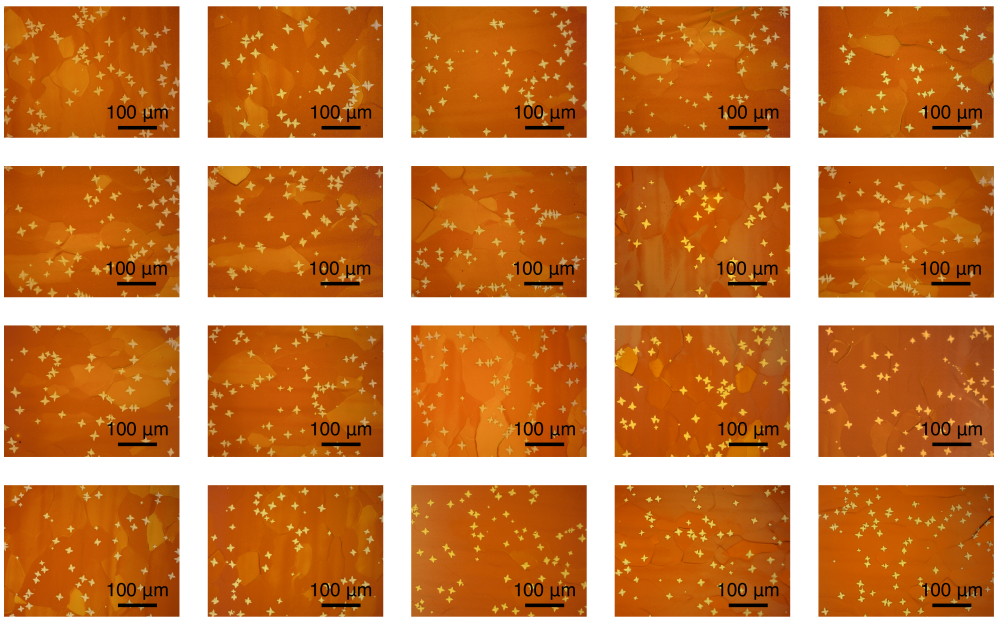

Fig. S4 20 repeated samples found in Figures 1d-e.

Comparison to other OF-CVD system

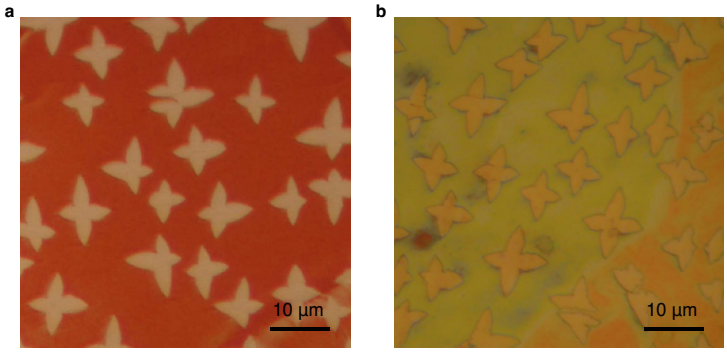

Fig. S5 H_2-free growth replicated in another synthesis system. a-b, H_2-free partial graphene growth from the OF-CVD system used for this work (at Columbia University) and an OF-CVD system at Infinite Potential Laboratories, respectively. Each sample started with the same Cu foil with identical surface pretreatment. The system at Infinite Potential Laboratories uses gas purification and purging of gas lines but has a different diameter (38.1 mm) and no load-lock. The synthesis in (**a**) was performed with the following conditions: $P_{CH_4} = 9.65$ mTorr, $P_{Ar} = 183$ mTorr, and $t_g = 1$ min. The synthesis in (**b**) was performed with the following conditions: $P_{CH_4} = 5$ mTorr, and $t_g = 1$ min. The Cu color difference between **a** and **b** can be attributed to varied hotplate oxidation time for graphene grain visualization.

Nucleation density is independent of t_g

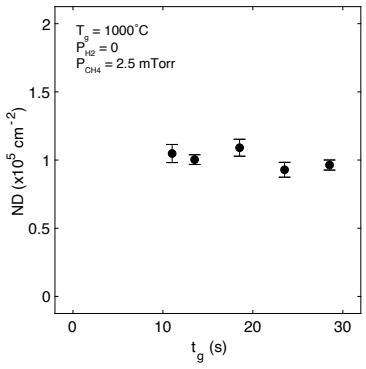

Fig. S6 Graphene grain nucleation density as function of t_g. Data presented is derived from the samples found in Figure 2b. This finding indicates that nucleation density does not vary with growth time, *i.e.* that the vast majority of nucleation events occur at the beginning of the growth step. Error bars indicate the standard deviation (1σ, n = 10)

Supplemental images for Figure 2a

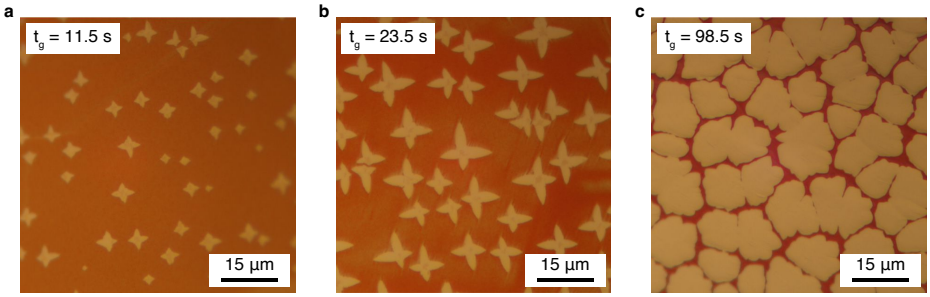

Fig. S7 Supplemental material for Figure 2a showing representative images of substrates at different stages of graphene growth. **a-c**, Images of substrates after growth with t_g = 11.5 seconds, 23.5 seconds, and 98.5 seconds with P_{CH_4} = 2.5 mTorr and P_{H_2} = 0.

Effect of P_{CH_4} and P_{H_2} on nucleation density

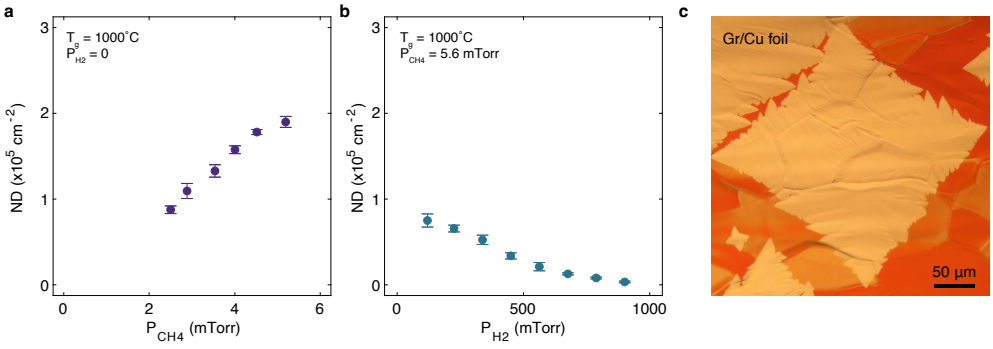

Fig. S8 Dependence of graphene grain nucleation density on gas composition. a, Nucleation density (number of graphene islands per area) vs. P_{CH_4}. **b**, nucleation density vs. P_{H_2}. Each data point within in this figure represents a distinct graphene sample. Error bars indicate the standard deviation (1σ, n = 10). Data presented is derived from the samples found in Figure 2d and 2e, respectively. **c**, Single graphene grain with $L > 300$ μm obtained by careful control of gas composition during synthesis.

The above panels show how the nucleation density (ND) is controlled by varying the methane and hydrogen partial pressures. ND increases monotonically with increasing P_{CH_4} (**a**), while ND decreases monotonically with increasing P_{H_2} (**b**). These trends are similar to those observed for the grain growth rate (Fig. 2d-e). We have used this control to grow large-grain ($L > 300$ μm) OF-CVD graphene on Cu foil (Fig. S8c). Growth parameters for **(c)** are the following: $T_g = 1050$ °C, $t_g = 60$ min, $P_{H_2} = 900$ mTorr, and $P_{CH_4} = 3$ mTorr.

Effect of methane purge on nucleation density

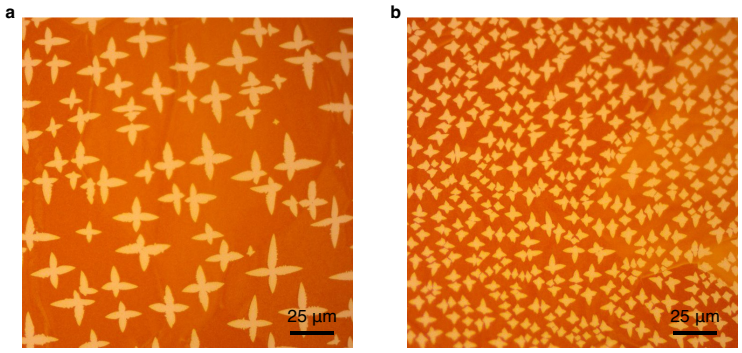

Fig. S9 Purging methane line prevents uncontrolled nucleation. Optical image of partial graphene growth (**a**) with and (**b**) without purge of space between the mass flow controller and the shutoff valve in the CH_4 flow line (Fig. 1a). Without the purge step, a short burst of CH_4 leads to high nucleation density.

Common mass flow controllers (MFCs) do not completely shut off gas flow when closed, and are therefore paired with a downstream shut-off valve. When gas flow is turned off, a small pocket of gas can build up in the space between the MFC and the valve. This pocket is then released when the flow is turned on, leading to a transient spike in flow above the nominal amount controlled by the MFC. Therefore, we pump out this section before turning on any gas.

Figure S9 compares graphene growth with and without purging of the CH_4 MFC. As shown in Figure S9a, the normal spontaneous nucleation is determined by the experimental conditions, i.e., temperature, P_{CH_4} and P_{H_2}. Intentionally disabling the bypass leads to a significant increase of ND (Fig. S9b) from 4.3×10^4/ cm^2 to 1.9×10^5/ cm^2. All other experimental conditions are kept the same except for the usage of the purge line.

Nucleation density and growth rate do not change with P_{Ar}

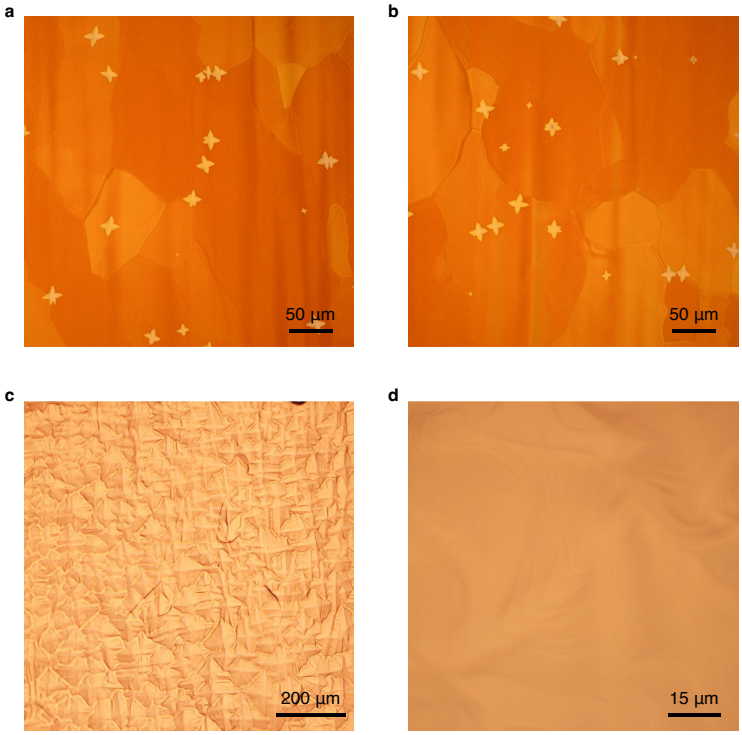

Fig. S10 Effect of Ar flow on graphene growth behavior. a-b, Optical image of graphene grains (at small t_g) grown with and without additional 40 sccm of Ar flow, respectively. No change in nucleation density or growth rate is observed. **c-d,** Optical images of a uniform graphene film with a pure Ar anneal step was included after t_g. The Ar anneal in (**c-d**) was performed with the following conditions: $P_{Ar} = 9$ Torr, $T_{anneal} = 1000$ °C, and $t_{anneal} = 30$ min.

We find that varying the Ar flow rate has no effect graphene growth. Figures S10a-b show optical images of two different samples in which (**a**) includes an additional 40 sccm of Ar flow during t_g. The effective growth behavior is very similar in terms of nucleation density and growth rate. Figures S10c-d show a full coverage graphene sample after a prolonged anneal in pure Ar at 1000 °C after t_g. We observe no etching of the graphene, indicating that our purified gas lines contain O_2 concentrations under the etching thresholds found in Figure 3.

Effect of H_2 on E_{app}

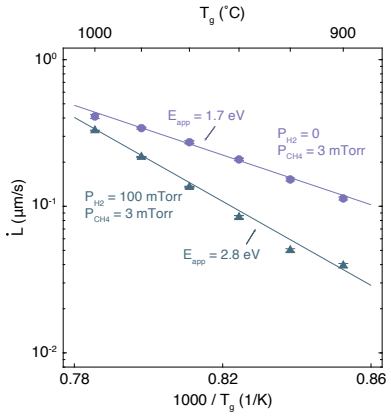

Fig. S11 Effect of H_2 on E_{app}. Arrhenius plot of growth rate with and without H_2. As in the main text (Fig. 2c), E_{app} is derived from the slope of each line. When H_2 is present (and $P_{H_2} >> P_{CH_4}$) (triangles), E_{app} is significantly larger than for the case of CH_4 only (circles). This indicates that the elementary reactions are different in the presence of hydrogen. Error bars indicate the standard deviation (1σ, n = 10).

Supplementary Note 2 - Compact model of graphene growth kinetics

The experimental evidence presented in the main text, which includes the proportionality between graphene growth and both the exposed Cu area and P_{CH_4}, along with the presence of four-fold grain shapes, suggests that the growth rate is governed by the carbon supply at the Cu surface. As detailed below, the carbon precursors are produced by a competitive reaction mechanism involving CH_4 and H_2 dissociative chemisorption at the surface of copper. Assuming equilibrium conditions, to the first order, the production of carbon precursors is related to two main competing reaction schemes:

$$CH_{4(g)} + 2S \overset{K_1}{\rightleftharpoons} CH_{3(ads)} + H_{(ads)} \tag{S2}$$

$$\frac{1}{2}H_{2(g)} + S \overset{K_2}{\rightleftharpoons} H_{(ads)} \tag{S3}$$

where S is a surface site for the reaction on copper, and $CH_{3(ads)}$ and $H_{(ads)}$ are the adsorbed methyl and hydrogen species on the copper surface, respectively. These reactions are competing because $H_{(ads)}$ is a reaction product in both processes.

The thermodynamic equilibrium constants for reactions S2 and S3 are:

$$K_1 = \frac{a_{CH_{3(ads)}} \cdot a_{H_{(ads)}}}{a_{CH_4} \cdot (a_S)^2} \tag{S4}$$

$$K_2 = \frac{a_{H_{(ads)}}}{\sqrt{a_{H_2}} \cdot a_S} \tag{S5}$$

where a_i is the activity of component i. Assuming ideal gas behavior at low pressure, the activity of each component is equal to its concentration(or partial pressure for gas phase species). This yields:

$$K_1 = \frac{[CH_3][H]}{P_{CH_4}[S]^2} \tag{S6}$$

$$K_2 = \frac{[H]}{\sqrt{P_{H_2}}[S]} \tag{S7}$$

According to the Le Chatelier principle, an increase of hydrogen pressure pushes the equilibrium and leads to a reduction of the concentration of methyl species on Cu. Hydrogen dissociation is therefore antagonistic to methyl generation and hence to graphene growth.

For the subsequent dehydrogenation steps, the quasi-steady-state approximation (QSSA) is assumed for the intermediate species in the following proposed graphene formation mechanism:

$$CH_{3(ads)} + S \overset{k_3}{\rightarrow} CH_{2(ads)} + H_{(ads)} \tag{S8}$$

$$CH_{2(ads)} + S \overset{k_4}{\rightarrow} CH_{(ads)} + H_{(ads)} \tag{S9}$$

$$CH_{(ads)} + S \xrightarrow{k_5} C_{(ads)} + H_{(ads)} \tag{S10}$$

$$C_{(ads)} \xrightarrow{k_6} C_{(graphene)} \tag{S11}$$

where k for each reaction is the forward reaction rate. We note that the proposed mechanism is one possible mechanism but not the only multi-step mechanism by which graphene can be formed.

Application of the QSSA allows the formation rates of the intermediate species to be set to zero, i.e., the intermediate species are consumed as fast as they are formed, hence:

$$r_{CH_{2(ads)}} = k_3[CH_3][S] - k_4[CH_2][S] = 0 \tag{S12}$$

$$r_{CH_{(ads)}} = k_4[CH_2][S] - k_5[CH][S] = 0 \tag{S13}$$

$$r_{C_{(ads)}} = k_5[CH][S] - k_6[C] = 0 \tag{S14}$$

$$r_{graphene} = k_6[C] \tag{S15}$$

The growth rate of graphene is then given by:

$$r_{graphene} = k_6[C] = k_3[CH_3][S] \tag{S16}$$

substituting for $[CH_3]$ using the equilibrium condition S6. Equation S16 becomes:

$$r_{graphene} = k_3 \cdot K_1 \cdot \frac{P_{CH_4}[S]^2}{[H]} \cdot [S] \tag{S17}$$

Substituting $[H]$ using the equilibrium condition S7 allows us to arrive at an expression for the rate of graphene formation:

$$r_{graphene} = k_3 \cdot \frac{K_1}{K_2} \cdot \frac{P_{CH_4}}{\sqrt{P_{H_2}}} \cdot [S]^2 \tag{S18}$$

The rate of graphene formation arrived at here is proportional to the graphene growth rate ($\dot{L}$) measured experimentally. $\dot{L}$ modelled here is the initial growth rate in equilibrium conditions. Importantly, $\dot{L}$ diverges when P_{H_2}=0, but this situation is not possible as the local P_{H_2} cannot be zero due to reactions S2 and S3. Because the local P_{H_2} cannot be measured in our setup, we consider only growth regimes when the applied P_{H_2} is larger than P_{CH_4}. Furthermore, the growth duration (t_g) is controlled so that the samples used to calculate the experimental $\dot{L}$ has approximately 10 % of graphene coverage. Together with the assumption of low surface adsorbates concentration, the $[S]^2$ term can be treated as a constant. In the situation where graphene coverage is high, a decrease of graphene growth rate is consistent with a decrease of $[S]$, as suggested by the model. Considering the assumptions made, k_3 can be seen as a rate limiting constant.

At equilibrium, the thermodynamic equilibrium constant K is related to the free energy of the surface reactions:

$$-RTln(K_j) = \Delta_r G^0 \tag{S19}$$

where K_j is the equilibrium constant of reaction j, R is the ideal gas constant, and T is the temperature.

As shown in Figure 2f (see main text), the experimental data collapse onto a linear function of $P_{CH_4}/\sqrt{P_{H_2}}$ similar to Eq. S18, with a slope of 1.455 ± 0.009 μm min^{-1} mTorr$^{1/2}$.

According to the model, the slope contains a ratio of equilibrium constants K_1/K_2. It is therefore interesting to note from Eq. S19:

$$\frac{K_1}{K_2} = \frac{e^{(-\Delta_r G^1/RT)}}{e^{(-\Delta_r G^2/RT)}} = e^{\left(-\frac{\Delta_r G^1 - \Delta_r G^2}{RT}\right)} \tag{S20}$$

where $\Delta_r G^1$ is the free energy of the methane chemisorption S2 and $\Delta_r G^2$ is the free energy for hydrogen chemisorption. It should be pointed out that this model neglects adsorbate-adsorbate interaction, and only involves the first step of methane dehydrogenation in the equilibrium assumption; the actual surface reaction is much more complex and may involve multiple rate limiting steps.

Further insight can be obtained from the model when considering the experimental ΔE_a for the growth rate is 1.7 ± 0.06 eV at $P_{H_2} = 0$, a regime with the fastest growth rates. The value of ΔE_a in the presence of extra H_2 is 2.8 ± 0.14 eV (See Figure S11). This higher value indicates an important change of equilibrium concentrations of the surface reaction intermediates when hydrogen pressure is applied.

While this model captures the essential mechanism at play, it probably neglects other important steps, and further understanding will therefore require more work. For simplicity, Eq. S18 can be slightly modified using *effective* equilibrium constants $K_{eq}^{CH_4}$ and $K_{eq}^{H_2}$ associated to the competing CH_4 and H_2 dissociation reactions on Cu as:

$$\dot{L} \propto \frac{K_{eq}^{CH_4}}{K_{eq}^{H_2}} \cdot \frac{P_{CH_4}}{\sqrt{P_{H_2}}} \tag{S21}$$

Lastly, these few kinetic and thermodynamic considerations provide a compact and simple model that can be used to guide graphene synthesis.

Residual gas analysis (RGA)

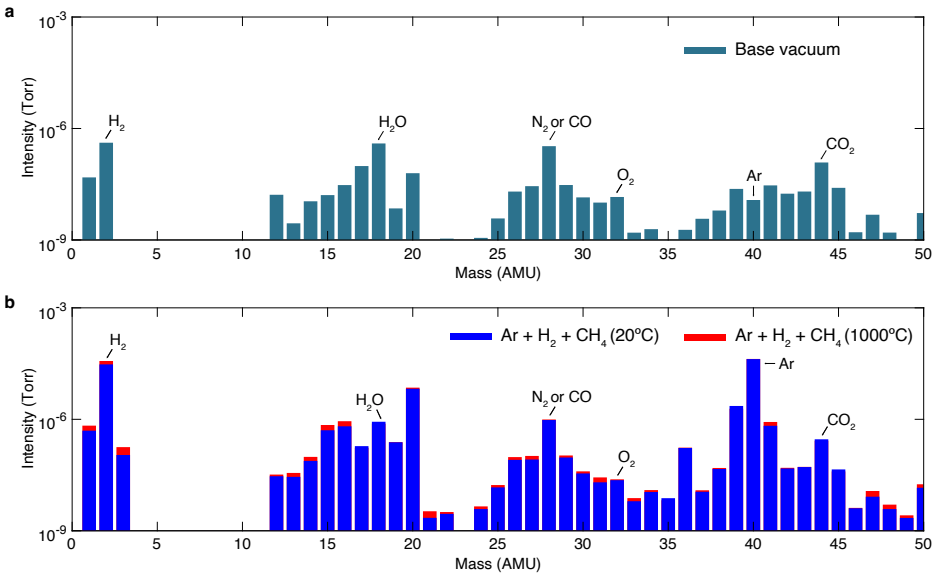

Fig. S12 RGA of OF-CVD system. **a**, RGA spectrum of OF-CVD graphene reactor measured at P_{base}. **b**, RGA spectrum of CVD graphene synthesis gas environment measured at both room temperature and T_g (1000°C).

We measured the gas composition within the the OF-CVD reactor using a residual gas analyzer (Stanford Research Systems, RGA-100). First, the system was baked at 150°C for 24 hours and pumped at room temperature until it reached P_{base} = 2.2 $\times 10^{-6}$ Torr. At P_{base}, the partial pressure of all oxygen containing species (H_2O, O_2, CO_2, and CO) are under the μTorr level with P_{O_2} = 1.4 $\times 10^{-8}$ Torr (Fig. S12a). We then implemented a sapphire-sealed variable leak valve (Kurt J. Lesker, AMLV1635CF) to create a typical OF-CVD graphene synthesis gas environment (P_{H_2} = 200 mTorr, P_{CH_4} = 4 mTorr, and P_{H_2} = 296 mTorr) within the RGA chamber ($P_{leak} \approx 1 \times 10^{-4}$ Torr). We note at both room temperature (20°C) and T_g (1000°C), P_{O_2} remains below $\approx 2 \times 10^{-8}$ Torr, confirming that no significant oxygen contamination arises from the gas sources or handling (Fig. S12b).

Oxygen pre-treatment delays nucleation

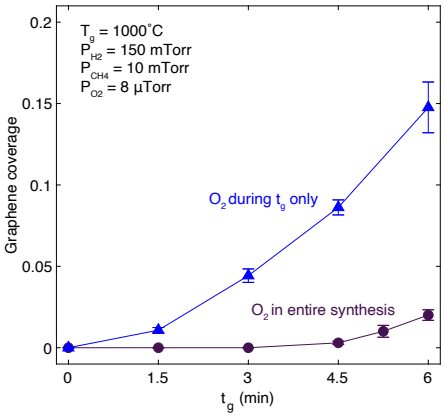

Fig. S13 Delayed nucleation with oxygen. Graphene coverage as a function of t_g where P_{O_2} = 8 μTorr was used in either the entire synthesis process (circles) or only during the growth phase (triangles). Error bars indicate the standard deviation (1σ, n = 10).

The data in Figure 3a show that trace oxygen causes a delay between the introduction of methane and graphene growth, indicating that the oxygen delays nucleation of graphene grains. To understand whether this effect arises from oxidation of the Cu surface, we examined early-stage grain growth for two cases: (1) addition of oxygen during the entire synthesis process; and (2) addition of oxygen simultaneously with methane during the growth phase. As can be clearly seen, the delay in grain nucleation occurs only for case (1). This indicates that oxidation of the Cu surface is likely responsible for delayed nucleation. This finding is in agreement with previous work [1] showing suppression of nucleation with oxygen.

Supplemental images for Figure 3a

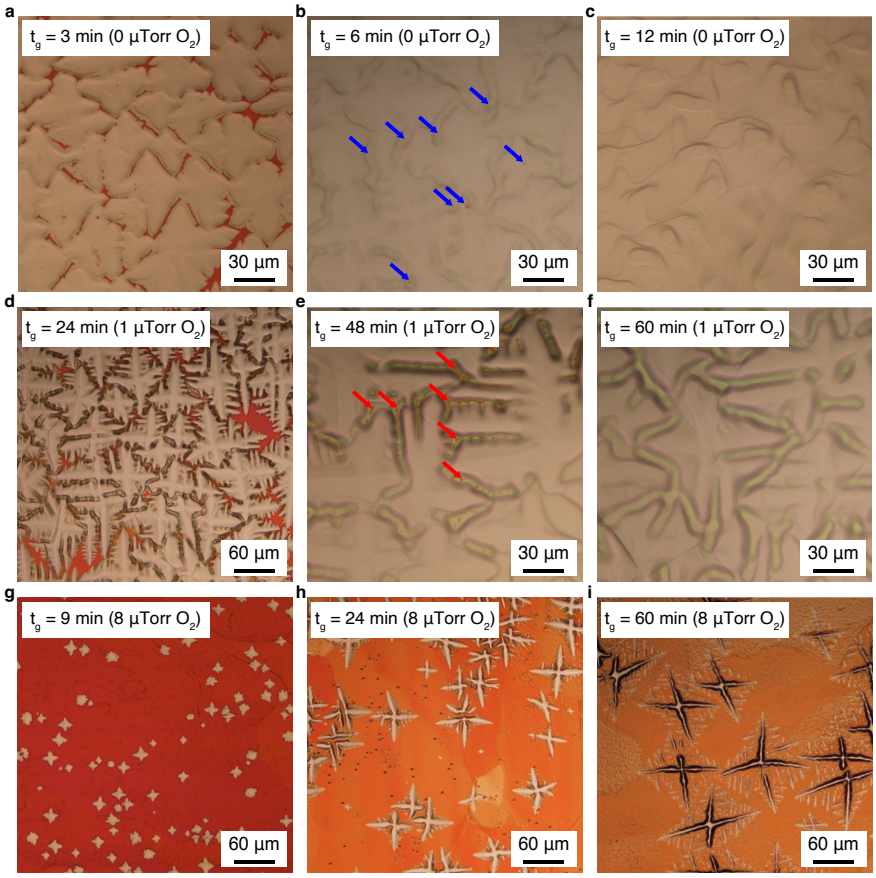

Fig. S14 Supplemental material for Figure 3a showing representative images of substrates at different stages of graphene growth for three levels of O_2. **a-c**, Images of substrates after growth with $t_g = 3$ minutes, 6 minutes, and 12 minutes with $P_{O_2} = 0$. Arrows on Figure S14b point to regions of exposed Cu. **d-f**, Images of substrates after growth with $t_g = 24$ minutes, 48 minutes, and 60 minutes with $P_{O_2} = 1$ μTorr. Arrows on Figure S14e point to exposed Cu. **g-i**, Images of substrates after growth with $t_g = 9$ minutes, 24 minutes, and 60 minutes with $P_{O_2} = 8$ μTorr.

Copper coating on tube as oxygen sink

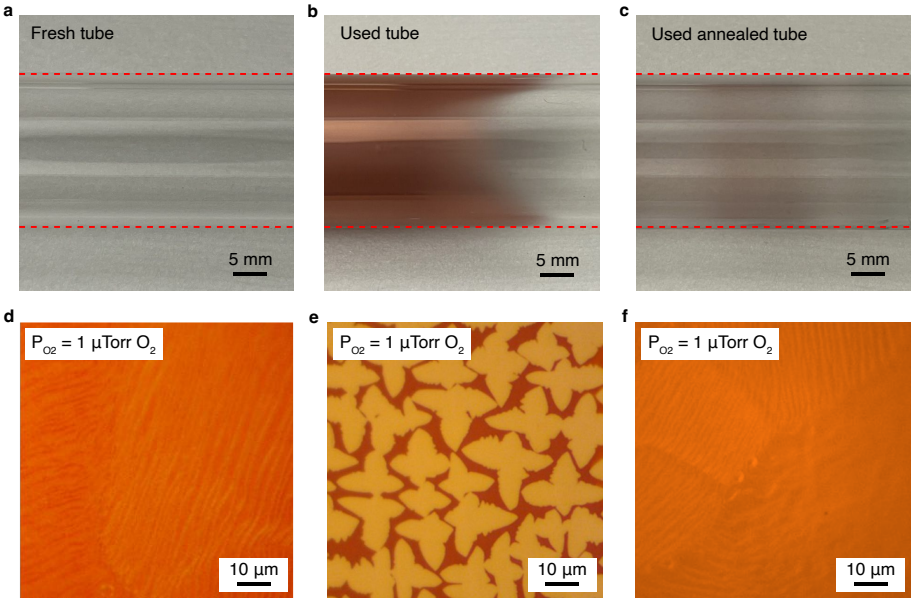

Fig. S15 Copper on growth tube acts as a sink for oxygen Optical images of the growth region of the quartz tube with the following conditions: **a**, fresh **b**, 100 growth cycles **c**, after annealing away the copper produced from Figure S15b. This is accomplished by first annealing the region at 1090 °C in pure H_2 to remove the most of the Cu followed by an 800 °C anneal in an environment of 1 % O_2 in Ar to convert any Cu to Cu_2O for prevent O_2 sinking. Red dashed lines indicate the quartz tube edge. **d**, The critical P_{O_2} to initially prevent graphene formation using a fresh quartz tube was found to be 1 μTorr. **e**, Once the tube walls is fully saturated with copper, introducing P_{O_2} = 1 μTorr was not enough to reproduce the results from Figure S15d pointing to oxygen sinking. **f**, After annealing the copper away P_{O_2} = 1 μTorr was enough to reproduce results from Figure S15d.

AFM characterization of surface contamination on Gr/Cu

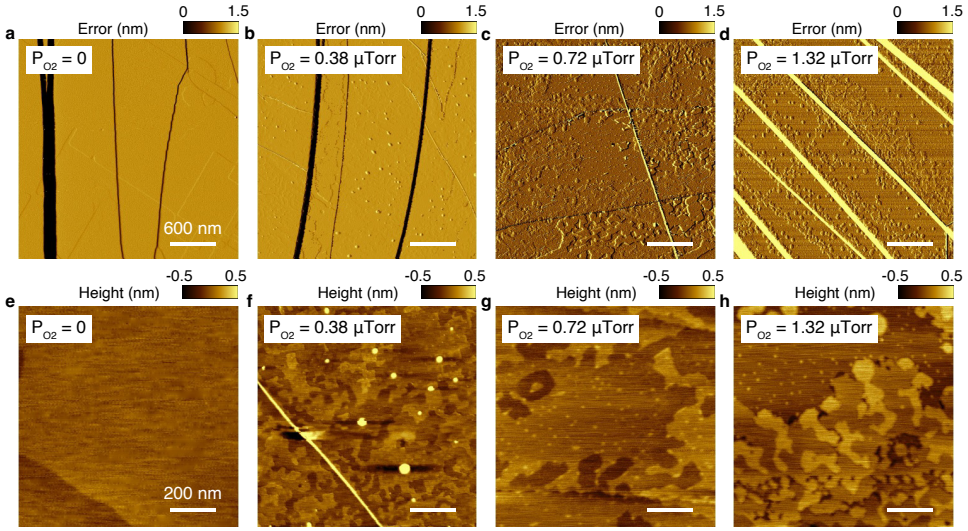

Fig. S16 AFM characterization of Gr/Cu surfaces. AFM is used to assess surface contamination for samples synthesized with various O_2 levels (Figure 3b-d) **a-d,** micron-scale maps of surfaces (scale bars 600 nm). At this scale, AFM error maps are used to most clearly resolve contamination. Straight lines are Cu step bunches. Contamination is seen with addition of O_2 as rough texture. **e-h,** Height maps of the graphene surface between Cu steps. Scale bars are 200 nm. Contamination is clearly observable with addition of O_2.

This figure shows AFM images of Gr/Cu foil samples used in Figure 3b-d. Images are obtained immediately after synthesis. In Figures S16a-d, AFM error maps show the distribution of the contamination on the graphene surface over micron scales despite the presence of tall Cu step bunches (straight lines) (contamination is not visible at this scale in AFM height maps). Zoomed-in height maps of areas between the copper step bunches clearly show the contamination on the graphene surface. The height of the contamination is less than 0.5 nm, with dot and web-like structures. This contamination is not seen in the O_2-free case.

Selective adsorption of Au

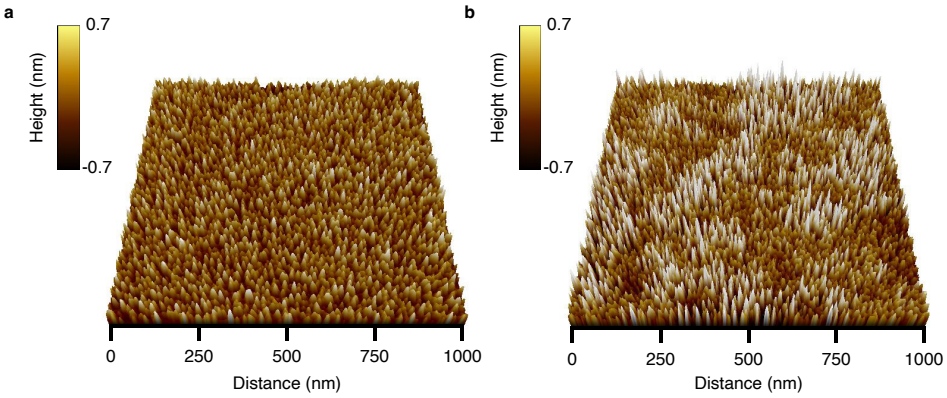

Fig. S17 Selective adsorption of Au on samples grown with O_2. AFM height images after deposition of 0.2 nm Au of gold on graphene grown on Cu foil (**a**) without and (**b**) with O_2.

Lin *et al.* [2] have shown that deposition of a thin layer of gold onto a graphene surface is an effective method to highlight surface contamination by amorphous carbon. Here we evaporate 0.2 nm onto the Gr/Cu surface using electron beam evaporation with a deposition rate of 0.01 nm/s. The growth conditions for (**a**) and (**b**) are identical to that of Figure 3(b, top left and right, respectively). Similar to [2], the Au adsorbs to contaminated regions with comparable distribution to the amorphous carbon seen in (Figs. 3 and S16).

Supplemental Raman mapping for Figure 3c

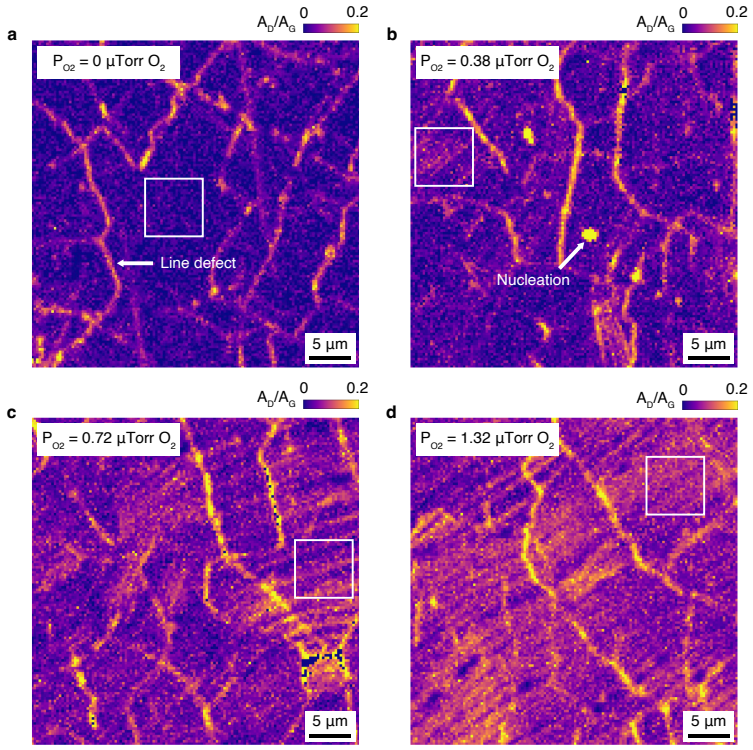

Fig. S18 Large-area Raman maps for samples shown in Fig. 3c. a-d, 40 μm × 40 μm maps of A_D/A_G for samples synthesized with varying P_{O_2} on polycrystalline Cu foil and wet-transferred to Si/SiO_2. Bright, narrow lines indicate line defects associated with grain boundaries and folds. The figures in the main text highlight areas between the folds/wrinkles, as indicated by the white boxes, in order to isolate the effect of trace O_2 on graphene defects. Raman characterization in Fig. S18a-d was collected with 532 nm excitation (N = 17,161).

In the above maps, the three most prominent features are line defects related to the grain boundaries from polycrystalline copper substrate, defective nucleation sites, and striations associated with amorphous carbon formation. In the main text (Fig. 3c), we restrict our analysis to regions without line and nucleation defects with a large striation density from each map to highlight effect of trace oxygen on amorphous carbon formation.

Control experiments for amorphous carbon contamination

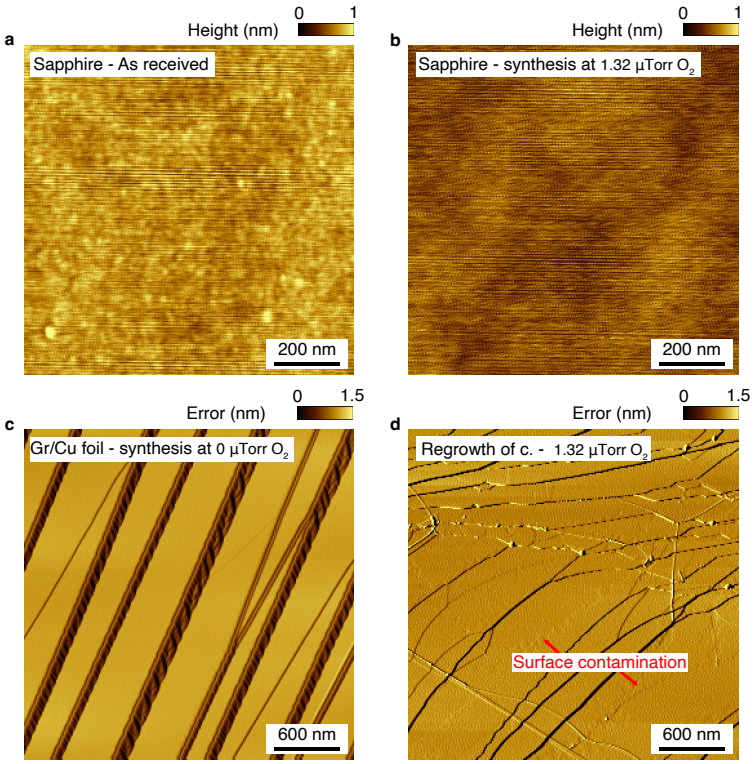

Fig. S19 Control experiments for amorphous carbon contamination. AFM height maps of sapphire surface (**a**) before and (**b**) after graphene synthesis conditions used to generate amorphous carbon found in Figure 3(b, top right). Neither shows any evidence of amorphous carbon accumulation. (**c**) AFM error map on Gr/Cu of OF-CVD graphene. (**d**) AFM error map of the sample in (**c**) after second growth cycle with 1.32 μTorr O_2. Surface contamination is indicated by the arrows

To provide better understanding regarding the origin of the amorphous carbon contamination observed in Figure 3, we performed a series of control experiments. We first subject a clean sapphire substrate to the same growth cycle as for graphene synthesis. As seen in AFM images before and after the (Fig. S19a-b), there is no increase in surface roughness and no evidence of contamination is seen. This suggests that the amorphous carbon contamination does not purely originate from gas-pyrolysis of CH_4 (which would cause uniform deposition on all surface).

As a second test, we grew graphene without O_2, yielding the clean surface shown in Fig. S19b. We then reintroduced the same sample to the chamber and repeated the growth cycle with $P_{O_2} = 1.32$ μTorr. After this process, the sample shows clear evidence of contamination (Fig. S19d). One possible explanation for these two findings is that oxygen-induced defects in the graphene are instrumental in accumulation of

amorphous carbon contamination. However, further study is needed to rigorously test this hypothesis.

Copper orientation study

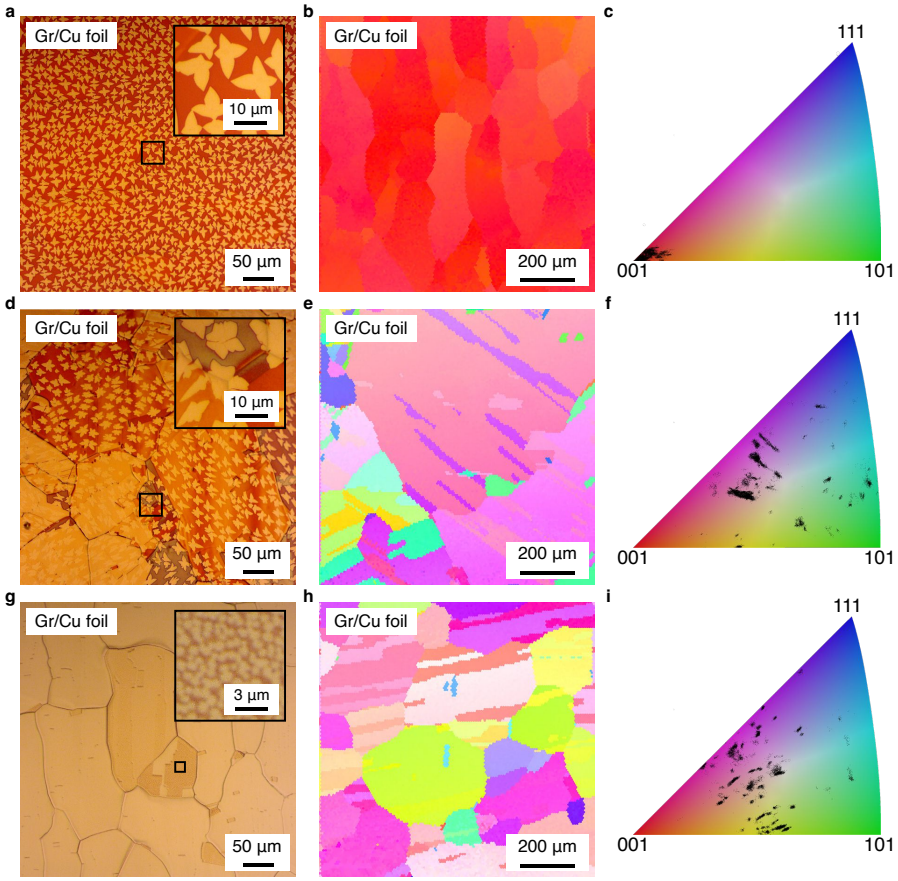

Fig. S20 Cu grain recrystalization and graphene nucleation using Cu foil from three different sources. Optical images of substrates after growth using **a**, Alfa-Aesar 46365 (Cu foil 1), **d**, Basic copper lot # 1mil-6inX10ft 99.9% pure (Cu foil 2), and **g**, Alfa-Aesar 10950 Cu foil, 0.025 mm thick, Puratronic, 99.999% (Cu foil 3). **b,e,h**, EBSD inverse pole figure (IPF) maps in the sample normal direction for Cu foil 1, 2, and 3, respectively. **c,f,i**, IPF with all present grain orientations overlaid for Cu foil 1, 2, and 3, respectively.

This figure illustrates the Cu and graphene grain structure after growth on electropolished Cu foils from three different sources. After graphene growth, Cu foil 1 shows uniform graphene nucleation and consistent recrystallization close to the (100) plane as seen in the electron backscatter diffraction (EBSD) map and inverse pole figure (IPF) plot. The graphene nucleation and grain shape is uniform on this surface. Because of this highly consistent behavior, Foil 1 was used for all of the other studies in this work. In contrast, Cu foils 2 and 3 contain a wide range of crystal orientations,

as confirmed by EBSD measurements. Nucleation density and grain size are similar for foils 1 and 2, but foil 3 shows a much higher nucleation density. High nucleation density can result from carbon impurities within the Cu [3].

Copper substrate characterization

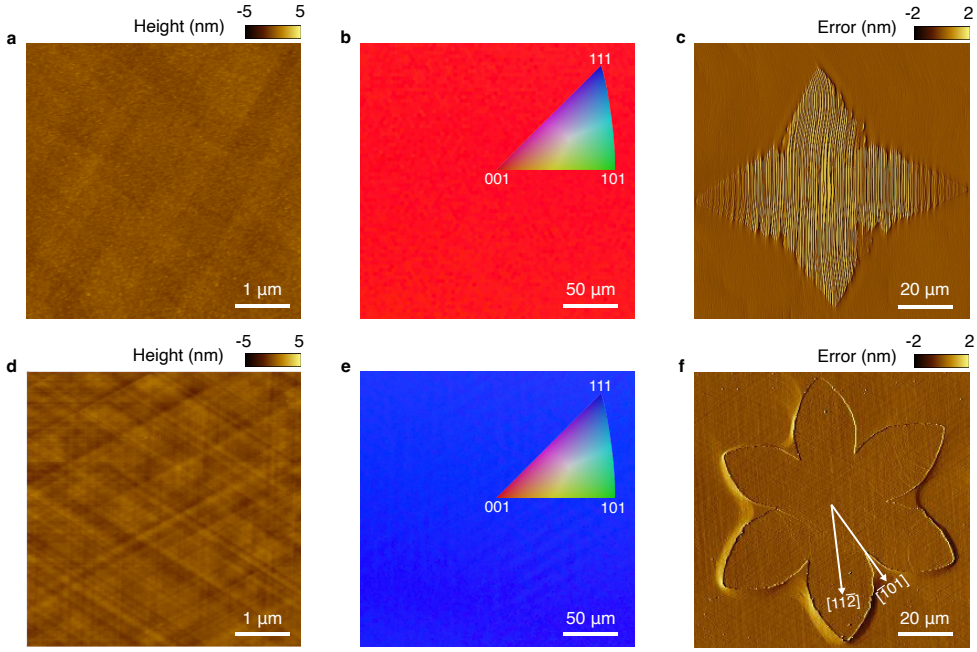

Fig. S21 Characterization of graphene synthesis substrates. a, d AFM surface topography of electropolished Cu foil and single-crystal Cu(111) film, respectively. **b, e** EBSD IPF maps in the sample normal direction for the Cu foil and film, respectively. The orientation keys are given as insets, with [001], [101], and [111] as directions in the crystal reference frame. **c, f** AFM error signal for graphene grains synthesized on Cu foil and film surfaces, respectively. Using X-ray diffraction, the fast growth directions of graphene in (**f**) are shown to be along $\langle 11\bar{2} \rangle$ directions of the Cu film.

Figure S21a is a typical AFM topography scan of the Cu foil surface after electropolishing (RMS roughness = 0.451 nm), the roughness is greatly reduced compared to the as-received condition. The recrystallization of the Cu grains can produce copper single crystal regions up to 200 μm (Fig. S21b). The crystal orientation of the copper foil used in this study is predominantly Cu(100), after growth, the graphene grains have a characteristic four-lobed shape, reflecting the crystal symmetry of the Cu(100) (Fig. S21c).

The copper thin film exhibits low roughness after annealing in H_2 at ambient pressure, with a surface RMS roughness of $\approx$ 0.2 nm (Fig. S21d). As confirmed by EBSD mapping, the crystal orientation is Cu(111) with single crystal domains without twinning (Fig. S21e). Graphene domains exhibit a six-lobed structure, as a result of diffusion-limited growth on Cu(111) surface. As shown in Figure S21f, the direction of the graphene domain high symmetry axis is aligned with the direction of copper atomic steps, which is the fast-diffusion direction of carbon on Cu(111).

It should be noted that the crystallinity of the Cu(111) thin film is extremely sensitive to the surface termination of sapphire substrate and interface cleanliness. To this end, the long-duration oxygen annealing step used here is necessary to avoid bi-crystal formation.

Cu(111) film uniformity after graphene growth

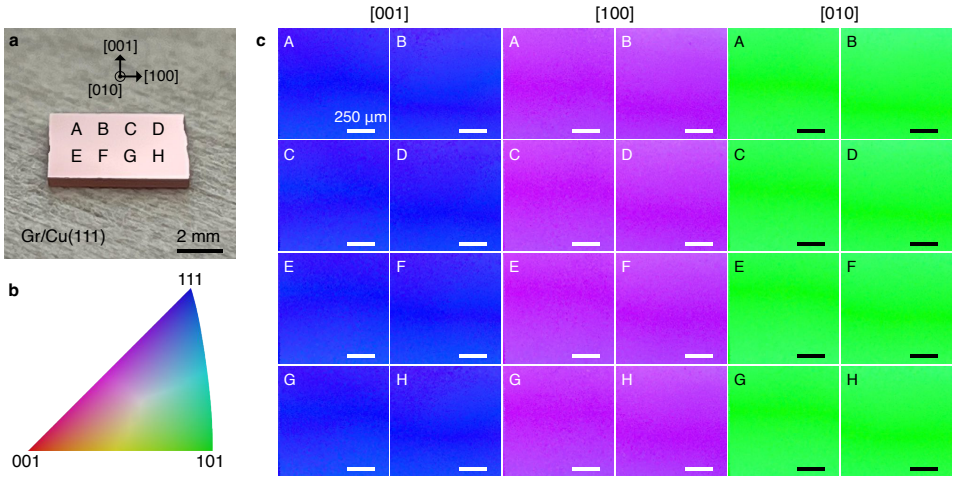

Fig. S22 EBSD mapping of Cu crystal orientation after growth of graphene on Cu(111). **a**, An optical image of the Gr/Cu sample surface with locations where the EBSD scans were taken. The specimen coordinate system for the EBSD measurement is overlaid on **a**. **b**, Crystal coordinate for the EBSD measurement. **c**, EBSD IPF maps in the sample normal and in-plane directions for the locations marked in **a**. All scale bars are 250 μm. The uniform blue color in the [100] direction indicates the dominant out-of-plane direction is (111), while the the uniform color maps in two corresponding in-plane directions [100] and [010] display in-plane orientation without twinning.

AFM study of surface topography of graphene on Cu(111)

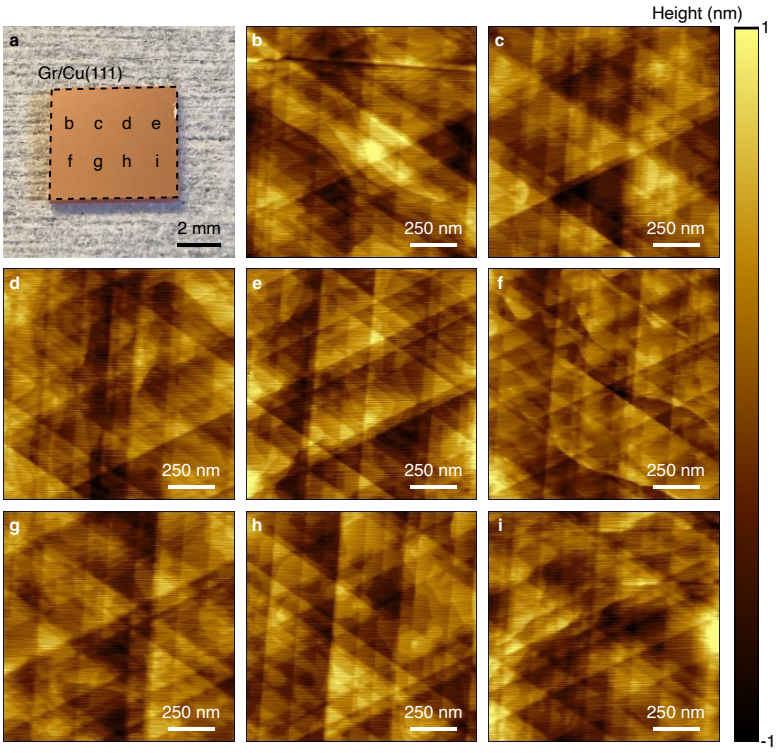

Fig. S23 AFM characterization of Gr/Cu(111) surface. a, An optical image of the Gr/Cu sample surface (black dotted lines) where the red dots show the locations where the AFM images were taken. **b-i**, AFM images obtained at these locations showing atomic Cu terraces. Note that all Cu steps are aligned pointing to a highly crystalline surface.

The Gr/Cu(111) surface was characterized with AFM immediately after growth. AFM height images were obtained from the sample at 8 different locations, all of which show aligned Cu atomic terraces, in agreement with EBSD measurements (Fig.S22). Additionally, no amorphous carbon contamination is oberved in any of the images.

STM study of surface topography of graphene on Cu(111)

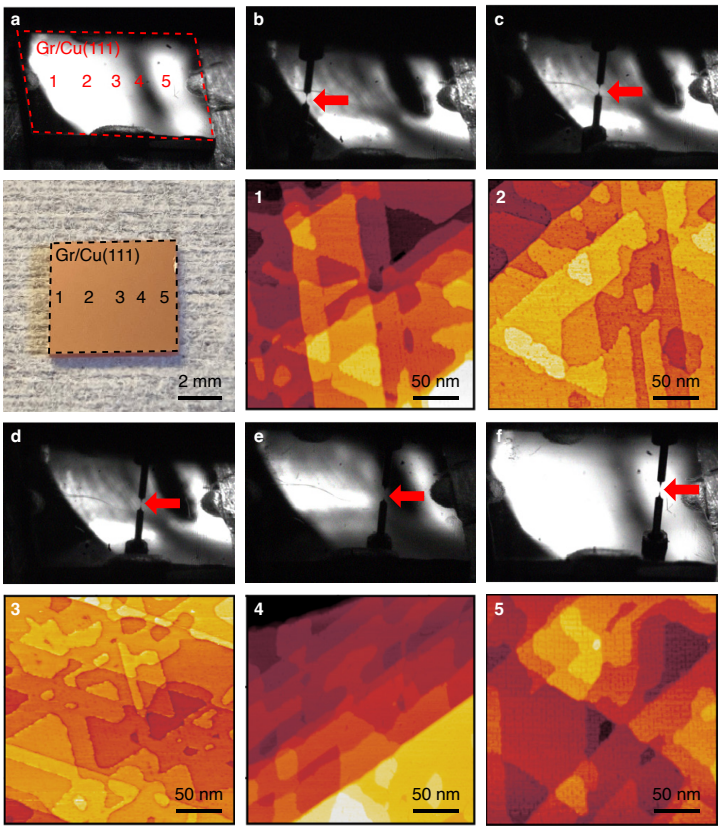

Fig. S24 STM characterization of Gr/Cu(111) surface. a, The top panel shows an optical image of the Gr/Cu sample surface (red dotted lines) with the bottom panel showing a corresponding optical image of the sample. The locations where the STM images were taken are labeled 1-5. **b-f** show an optical image of the sample with a red arrow indicating the location of the STM tip. The bottom panels show STM images obtained at these locations with a sample bias of 1 V and set point current of 100 pA.

We performed STM measurements along an approximately centimeter range at five different locations on the surface. Although STM is a local technique, measurements obtained across a large spatial range of the sample can aid in showing the cleanliness of the growth. Shown in the top of Figure S24a is an optical image of the Gr/Cu(111) surface in the STM, and below is a graphic with red dots indicating the location where each of the STM images was obtained. Figures S24b-f show an optical image of the STM tip with the reflection on the Gr/Cu surface, indicated by the red arrow to show where the measurement was taken. The bottom panels of Figures S24b-f are the STM images obtained at each of the locations, demonstrating clear flat terraces

from the Cu(111) substrate. At each of the locations across the surface, we see that the Cu(111) terraces are rotationally aligned, and the spots from the moiré pattern of the graphene and Cu(111) lattices are visible. Although the STM images were taken millimeters apart, the sample quality is consistent. Notably, there is no evidence of amorphous carbon on the surface.

Water-assisted oxidation of Cu(111) after graphene growth

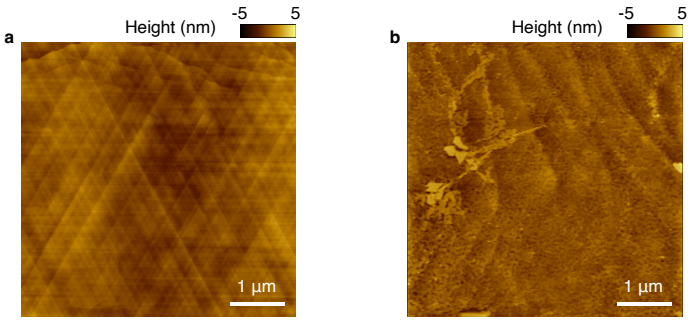

Fig. S25 Water-vapor-assisted oxidation of Gr/Cu for dry assembly. a-b, AFM topography of the Gr/Cu surface before and after 12 h of oxidation at 75 °C, respectively.

To avoid surface contamination involved in conventional wet transfer process, we perform dry transfer of graphene. In this process, the graphene is directly picked up by h-BN from the Cu(111) substrate. The oxidation of copper is necessary to weaken the adhesion of between graphene and the substrate. To achieve sufficient oxidation, while preserving the flat surface of the Cu(111) single crystal, the sample is placed in an enclosure filled with air saturated with water vapor at 75 °C for 12 h. After oxidation, the surface roughness only increased by a small amount (Fig. S25b).

It should be noted that the oxidation initiates only from the defect sites in the graphene. As a result, the oxide formation in the interface for high quality graphene is very slow, and the oxide thickness distribution is uneven as a result of the slow transport of water in the interface. Therefore, even though this method successfully yields flat areas on the scale of tens of microns suitable for for device fabrication, achieving uniform oxidation over larger areas will require further investigation.

Raman mapping of graphene on various substrates

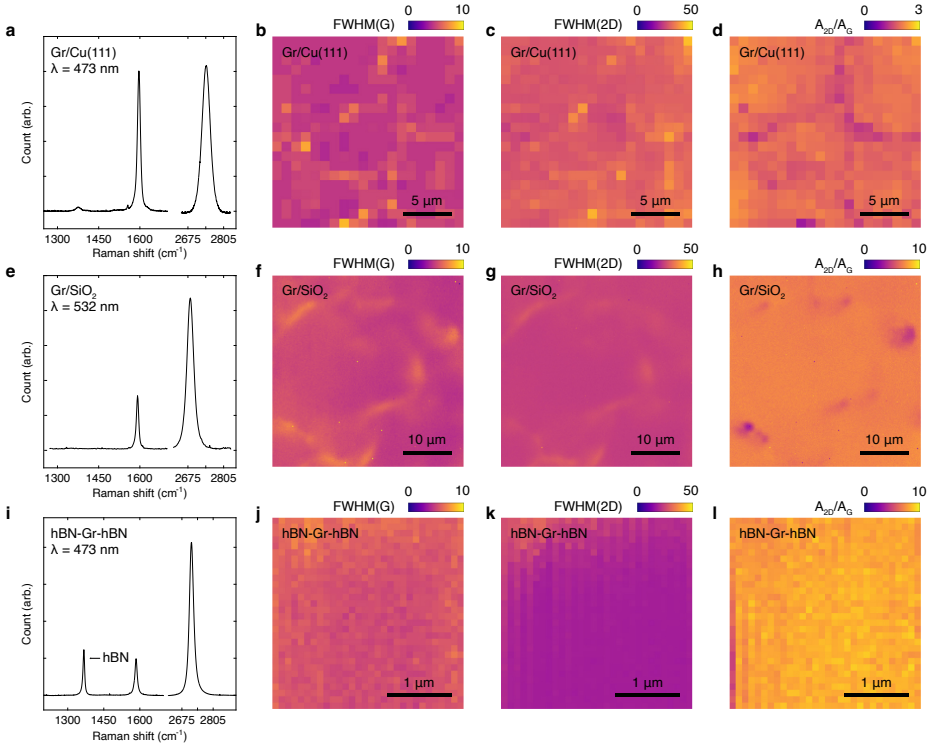

Fig. S26 Raman analysis of graphene grown on Cu(111) on various substrates. a, Averaged Raman spectra of graphene on Cu(111) collected with 473 nm excitation (N = 441). **b-d,** Raman mapping of FWHM(G), FWHM(2D), and A_{2D}/A_G for graphene on Cu(111). **e,** Averaged Raman spectra of graphene on SiO_2 collected with 532 nm excitation (N = 26,896). **f-h,** Raman mapping of FWHM(G), FWHM(2D), and A_{2D}/A_G for graphene on SiO_2. **i,** Averaged Raman spectra of hBN-encapsulated graphene collected with 473 nm excitation (N = 1,380). **j-l,** Raman mapping of FWHM(G), FWHM(2D), and A_{2D}/A_G for hBN-encapsulated graphene.

Table S2 Average Raman mapping values

Sample	FWHM(G) (cm^{-1})	FWHM(2D) (cm^{-1})	A_{2D}/A_G
Gr/Cu(111)	9.6 ± 1.2	29.5 ± 2.7	1.9 ± 0.2
Gr/SiO_2	10.1 ± 0.9	24.3 ± 0.8	6.8 ± 0.3
hBN-encapsulated Gr	11.1 ± 0.8	19.2 ± 2.2	8 ± 0.4

Electrical characterization of graphene transferred on Si^{++}/SiO_2

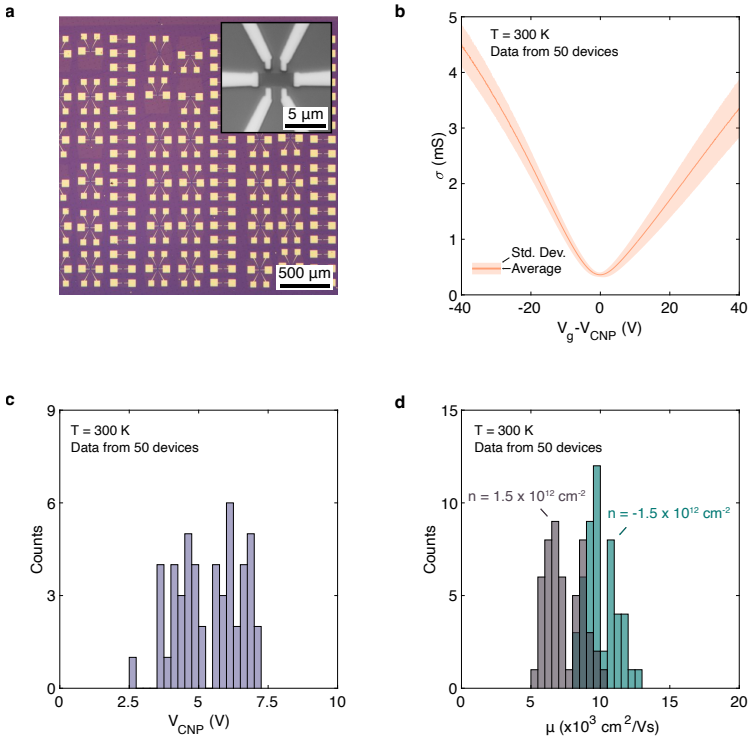

Fig. S27 Electrical characterization of wet-transferred graphene on Si^{++}/SiO_2. a, Optical image of 2 and 4-probe graphene devices. Inset of **(a)** shows Hall bar structure. **b,** Averaged room-temperature conductivity (σ) versus V_g-V_{CNP} for 50 4-probe graphene devices. The SiO_2 thickness is 285 nm. Histogram showing the spread of the **(c)** charge neutrality voltage (V_{CNP}) and **(d)** room-temperature mobility (μ) measured at $n = \pm 1.5 \times 10^{12}$ cm^{-2}.

To construct devices on Si^{++}/SiO_2 substrates, a continuous layer of graphene synthesized on Cu foil was first wet-transferred to the Si/SiO_2 using the Paraffin/PMMA technique found in Methods. The SiO_2 thickness was 285 nm. Device regions were chosen at random to assess homogeneity across the surface. The array of graphene Hall bars shown in Fig. S27a was fabricated using the lithographic steps found in Methods. The sample was loaded into a vacuum pump station and pumped overnight prior to measurement ($P_{base} = 2 \times 10^{-6}$ Torr). All measurements had the following conditions: $T = 300$ K, $V_g = \pm 40$ V, and $V_{ds} = 100$ mV. The average position of the charge neutrality pont (V_{CNP}) for 50 devices was 5.34 $\pm$ 1.14 V (Fig. S27c). The data shown in Figure S27b are converted to mobility using $\mu = \frac{\sigma}{|n|e}$, where $n = C_g(V_g - V_{CNP})/e$ is the net carrier density induced by the gate, and C_g is the

gate capacitance per unit area. The 50 devices show hole mobility of 10,030 ± 1,120 cm^2/Vs at $n = -1.5 \times 10^{12}$ cm^{-2} and electron mobility of 7,398 ± 1,281 cm^2/Vs at carrier concentration of $|n| = 1.5 \times 10^{12}$ cm^{-2} (Fig. S27d).

hBN-encapsulated devices

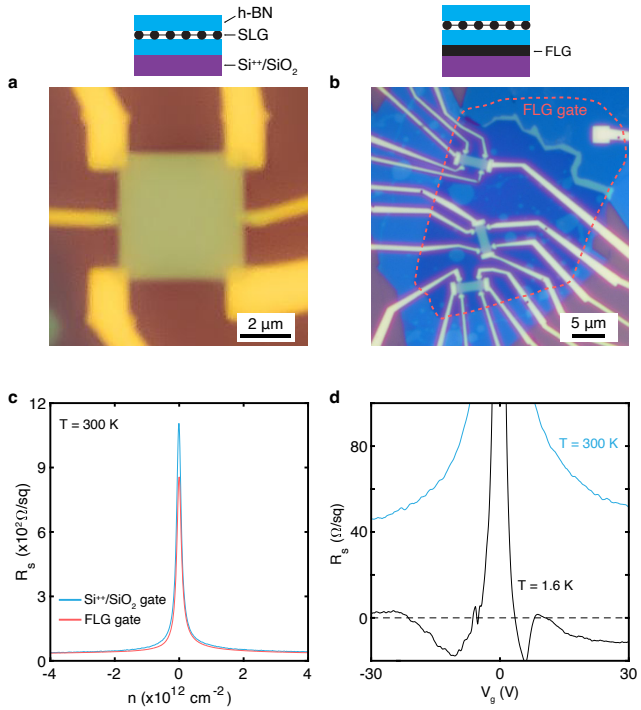

Fig. S28 hBN-encapsulated devices (**a**) Optical image of hBN-encapsulated OF-CVD graphene device on Si^{++}/SiO_2 substrate. A van der Pauw contact configuration is used as shown. (**a**) Optical image of devices with few-layer-graphite (FLG) back-gate, with Hall bar configuration. **c,** Room-temperature sheet resistance as a function of density for both devices seen in S28a-b. **d,** Low-temperature sheet resistance for the Si^{++}/SiO_2 gated device. Negative resistance in the van der Pauw geometry indicates ballistic transport.

The hBN-encapsulated devices were fabricated using the polymer-free dry pickup technique found in Methods. The thickness of each hBN layer was approximately 30 nm and the exfoliated graphite gate used panel **(b)** was 10 nm thick.

Sheet resistivity and Hall mobility calculation in van der Pauw configuration

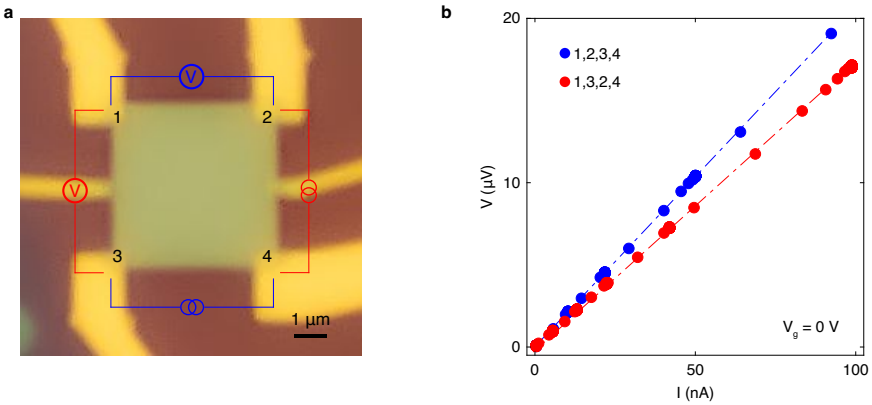

Fig. S29 Van der Pauw corrections for sheet resistance. a, Optical image of BN-encapsulated CVD graphene device with overlaid measurement configurations. **b,** I-V curves for horizontal and vertical measurement configurations. Graphene used for this device was transferred directly from Cu_2O using the polymer-free technique outlines in Methods.

The sheet resistance, R_s, of the BN/Gr/BN structure was measured similar to with details described here. Consider the device with edge contacts along the periphery (Fig. S29a). The four-terminal resistance (vertical configuration) is defined as

$$R_{1,2\ 3,4} = \frac{V_{12}}{I_{34}} \tag{S22}$$

where I_{34} flows from contact 3 to contact 4 being sourced by a lock-in amplifier output at a frequency of 17 Hz. $V_{12} = V_1 - V_2$ is the voltage difference between contacts 1 and 2, measured by the same lock-in amplifier in differential mode. $R_{1,3\ 2,4}$ (horizontal configuration) is defined similarly as V_{13}/I_{24}. We collect output profiles for each configuration at a back gate voltage of 0 V (Fig. S29b). This provides values for $R_{1,2\ 3,4}$ and $R_{1,3\ 2,4}$ to extract the sheet resistance at $V_g = 0$ V at room temperature via the van der Pauw relation

$$e^{-\pi R_{1,2\ 3,4}/R_s} + e^{-\pi R_{1,3\ 2,4}/R_s} = 1 \tag{S23}$$

to give us an approximated sheet resistance as 4.14 x $R_{1,2\ 3,4}$.

Carrier mobility μ (Figure 4e) was calculated using $\sigma = \frac{1}{R} = ne\mu$, where n is the net carrier density defined as $n = C_i(V_g - V_{CNP})/e$ with the gate-channel capacitance defined by $C_i = (C_{hBN}C_{SiO_2})/(C_{hBN} + C_{SiO_2})$. We note that this model is valid only when $n >> n^*$, where n^* represents the broadening of the Dirac peak due to charge disorder and thermal excitation of carriers.

Activation gap analysis

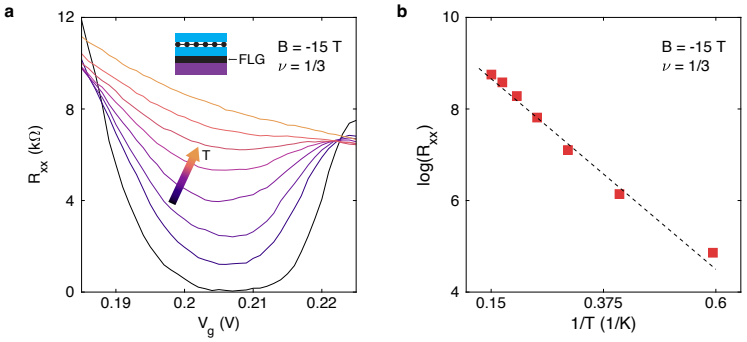

Fig. S30 Activation gap measurements. a, R_{xx} as a function of V_g and temperature for the $\nu = 1/3$ state. **b,** Minimum R_{xx} of the 1/3 state as function of inverse temperature (1/T) at a constant magnetic field of -15 T. The dashed line shows a fit of the temperature activated model $R_{xx} = Re^{(-\Delta_\nu/2k_BT)}$.

Quantum scattering time and Landau level broadening

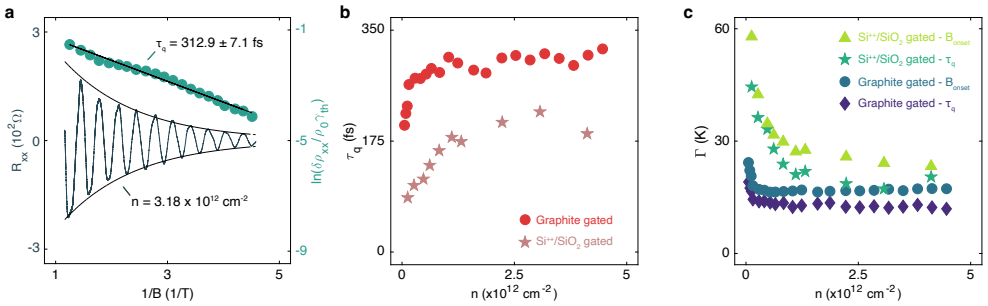

Fig. S31 **a,** Shubnikov-de Haas oscillation and Dingle plot for the graphite gated device measured at carrier density $n = 3.18 \times 10^{12}$ cm^{-2}. **b,** τ_q as a function of carrier density for both Si^{++}/SiO$_2$ and graphite gating. The saturation of τ_q with increasing density is expected. **c,** Landau level broadening Γ, extracted from quantum lifetime τ_q and the onset of SdH oscillations vs. carrier density n for both Si^{++}/SiO$_2$ and graphite gating. Graphene used for these devices was dry-transferred directly from the oxidized Cu(111) substrate using the polymer-free technique outlines in Methods.

The quantum scattering time τ_q is derived from the Dingle plot shown in Figure S31a. In this plot, the longitudinal resistance R_{xx} is plotted as a function of inverse magnetic field B^{-1}. The normalized oscillation amplitude $\Delta\rho_{xx}/\rho_0\gamma_{th}$ is then plotted on a log scale, with

$$\Delta\rho_{xx}/\rho_0\gamma_{th} = 4exp(-\pi/\omega_c\tau_q) \tag{S24}$$

where $\gamma_{th} = (2\pi^2 k_B T/\hbar\omega_c)/sinh(2\pi^2 k_B T/\hbar\omega_c)$ is the Dingle term, and τ_q is the quantum scattering time. The cyclotron frequency is $\omega_c = eB/m^*$, with effective mass given by $m^* = \hbar\sqrt{n\pi}/(V_F m_e)$ The fitted slope gives $\tau_q = 312.9 \pm 7.1$ fs.

Figure S31b shows the measured value of τ_q as a function of electron density n for the hBN-encapsulated samples on SiO$_2$ (Fig. 3d,e) and with the graphite back-gate (Figs. 3f-j). At lower density, remote scattering from charge disorder in the Si^{++}/SiO$_2$ substrate decreases quantum lifetime. Figure S31c shows the Landau level broadening Γ as a function of density. Γ is derived from τ_q by $\Gamma = \hbar/2\tau_q$. A second estimate of Γ is provided from the onset of SdH oscillations by $\Gamma = v_f\sqrt{2e\hbar B_{onset}}(\sqrt{|\ N\ |} - \sqrt{|\ N-1\ |})$ where the Fermi velocity in graphene is $v_f = 1\times10^6$ m/s and $N = \frac{nh}{4eB} - 0.5$.

Comparison of electrical transport measurements to literature

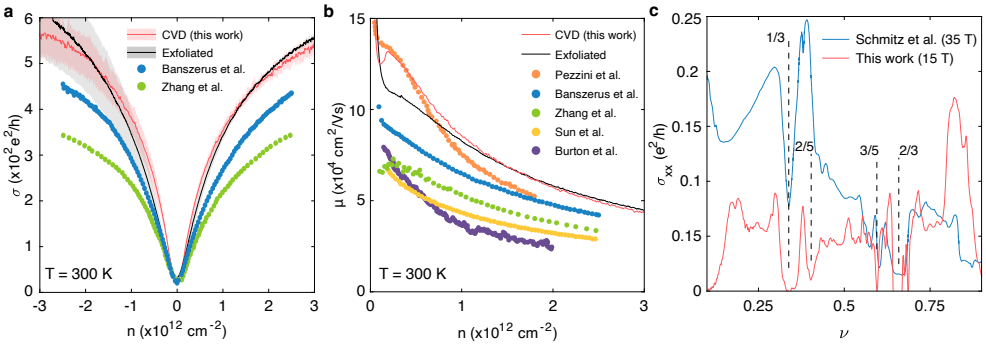

Fig. S32 Comparison of electrical transport in OF-CVD graphene with other CVD graphene in the literature. a, Room-temperature conductivity (σ) versus net carrier density density, compared to exfoliated graphene (Fig. 4e) and data shown in Banszerus et al. [4] and Zhang et al. [5]. **b,** Room-temperature mobility versus electron density for OF-CVD graphene compared to the same works as in (a), in addition to Pezzini et al. [6], Sun et al. [7], and Burton et al. [8]. The data shown in (a) is converted to mobility using $\mu = \frac{\sigma}{ne}$. While average electron and hole conductivities are similar, larger variability (both for CVD and exfoliated devices) is seen on the hole side. Therefore we focus only on electron mobility. **c,** Comparison of fractional quantum Hall effect in OF-CVD graphene with data from recent observation of FQHE in CVD graphene (Schmitz et al. [9]) Data shows σ_{xx} vs. filling fraction ν for $0 < \nu < 1$. Both data sets show minima in σ_{xx} at fractional values of ν. However, the data for OF-CVD show $\sigma_{xx} = 0$, whereas the previous report does not achieve $\sigma_{xx} = 0$ even at $B = 35$ T.

References

[1] Hao, Y., Bharathi, M.S., Wang, L., Liu, Y., Chen, H., Nie, S., Wang, X., Chou, H., Tan, C., Fallahazad, B., Ramanarayan, H., Magnuson, C.W., Tutuc, E., Yakobson, B.I., McCarty, K.F., Zhang, Y.W., Kim, P., Hone, J., Colombo, L., Ruoff, R.S.: The role of surface oxygen in the growth of large single-crystal graphene on copper. Science **342**(6159), 720–723 (2013) https://doi.org/10.1126/science.1243879

[2] Lin, L., Zhang, J., Su, H., Li, J., Sun, L., Wang, Z., Xu, F., Liu, C., Lopatin, S., Zhu, Y., Jia, K., Chen, S., Rui, D., Sun, J., Xue, R., Gao, P., Kang, N., Han, Y., Xu, H.Q., Cao, Y., Novoselov, K.S., Tian, Z., Ren, B., Peng, H., Liu, Z.: Towards super-clean graphene. Nature Communications 2019 10:1 **10**(1), 1–7 (2019) https://doi.org/10.1038/s41467-019-09565-4

[3] Braeuninger-Weimer, P., Brennan, B., Pollard, A.J., Hofmann, S.: Understanding and Controlling Cu-Catalyzed Graphene Nucleation: The Role of Impurities, Roughness, and Oxygen Scavenging. Chemistry of Materials **28**(24), 8905–8915 (2016) https://doi.org/10.1021/acs.chemmater.6b03241

[4] Banszerus, L., Schmitz, M., Engels, S., Dauber, J., Oellers, M., Haupt, F., Watanabe, K., Taniguchi, T., Beschoten, B., Stampfer, C.: Ultrahigh-mobility graphene devices from chemical vapor deposition on reusable copper. Science Advances **1**(6) (2015) https://doi.org/10.1126/sciadv.1500222

[5] Zhang, J., Jia, K., Huang, Y., Liu, X., Xu, Q., Wang, W., Zhang, R., Liu, B., Zheng, L., Chen, H., Gao, P., Meng, S., Lin, L., Peng, H., Liu, Z.: Intrinsic Wettability in Pristine Graphene. Advanced Materials **34**(6), 2103620 (2022) https://doi.org/10.1002/adma.202103620

[6] Pezzini, S., Mišeikis, V., Pace, S., Rossella, F., Watanabe, K., Taniguchi, T., Coletti, C.: High-quality electrical transport using scalable CVD graphene. 2D Materials **7**(4), 041003 (2020) https://doi.org/10.1088/2053-1583/aba645

[7] Sun, L., Chen, B., Wang, W., Li, Y., Zeng, X., Liu, H., Liang, Y., Zhao, Z., Cai, A., Zhang, R., Zhu, Y., Wang, Y., Song, Y., Ding, Q., Gao, X., Peng, H., Li, Z., Lin, L., Liu, Z.: Toward Epitaxial Growth of Misorientation-Free Graphene on Cu(111) Foils. ACS Nano **16**(1), 285–294 (2022) https://doi.org/10.1021/acsnano.1c06285

[8] Burton, O.J., Winter, Z., Watanabe, K., Taniguchi, T., Beschoten, B., Stampfer, C., Hofmann, S.: Putting High-Index Cu on the Map for High-Yield, Dry-Transferred CVD Graphene. ACS Nano **17**, 1229–1238 (2022) https://doi.org/10.1021/acsnano.2c09253

[9] Schmitz, M., Ouaj, T., Winter, Z., Rubi, K., Watanabe, K., Taniguchi, T., Zeitler, U., Beschoten, B., Stampfer, C.: Fractional quantum Hall effect in CVD-grown graphene. 2D Materials **7**(4), 041007 (2020) https://doi.org/10.1088/2053-1583/ABAE7B